Advanced Fiber Materials
https://doi.org/10.1007/s42765-026-00774-3

RESEARCH ARTICLE

Ultrasoft Core–Shell Inorganic Nanoyarns for Energy and Sensing Applications

Dabin Kim[1] · Suchithra Padmajan Sasikala[2] · Ji-Hwan Ha[3] · Oh-Sung Kwon[4] · Jungrak Choi[5] · Yongrok Jeong[6] · Hanhwi Jang[2] · Jun-Ho Jeong[7] · Zhi-Jun Zhao[8] · Inkyu Park[9] · Sangouk Kim[2] · Junseong Ahn[1]

Received: 27 March 2026 / Accepted: 28 July 2026
© Donghua University, Shanghai, China 2026

Abstract

Inorganic nanoyarns with high electrical conductivity, tunable redox activity, and outstanding chemical/thermal stability are promising components for high-performance multifunctional fibers. However, integrating inorganic functionality with the softness, durability, and processability required for wearable fiber systems remains a major challenge. Here we present ultrasoft core–shell nanoyarns composed of inorganic nanoribbon cores and polymer shells with exceptional mechanical compliance while maintaining high electrical and chemical performance. The inorganic core provides multifunctionality and structural diversity with single-layer, particle-decorated, and multilayer sandwich architectures. A grounded-core electrospinning strategy is introduced to form porous polymer shells around the inorganic cores, providing mechanical reinforcement, electrical insulation, and diffusion pathways for reactive species within a resilient, flexible framework. The proposed core–shell nanoyarns function as efficient water-splitting electrodes, deliver a high volumetric energy density in fiber-type supercapacitors, and operate as force sensors capable of detecting forces at the tens-of-micronewton level. These results establish the core–shell nanoyarn as a universal and scalable platform for wearable energy and sensing systems.

Keywords Core–shell nanoyarns · Inorganic nanoribbons · Electrospinning · Water-splitting · Fiber supercapacitors · Wearable sensors

1 Introduction

Smart textiles aim to realize intimate human–machine interfaces and self-powered electronic devices, while offering stable operation and functional durability under wearable or dynamically deformable conditions [1–4]. Despite the rapid progress in flexible and wearable electronics, either typical planar or thin-film devices cannot accommodate diverse and complex modes of mechanical deformation [5–8]. In this regard, nano-structured inorganic yarns that can effectively translate nanoscale physical attributes, such as high surface-area-to-volume

Dabin Kim, Suchithra Padmajan Sasikala, and Ji-Hwan Ha have contributed equally to the work.

✉ Inkyu Park
inkyu@kaist.ac.kr

✉ Sangouk Kim
sangouk@kaist.ac.kr

✉ Junseong Ahn
junseong@korea.ac.kr

[1] Department of Control and Instrumentation Engineering, Korea University, Sejong 30019, Republic of Korea

[2] Department of Materials Science and Engineering, Korea Advanced Institute of Science and Technology (KAIST), Daejeon 34141, Republic of Korea

[3] Department of Mechanical Engineering, Hanbat National University, Daejeon 34158, Republic of Korea

[4] Department of Electro-Mechanical Systems Engineering, Korea University, Sejong 30019, Republic of Korea

[5] Electronics and Telecommunications Research Institute (ETRI), Daejeon 34129, Republic of Korea

[6] School of Mechanical Engineering, Kyungpook National University, Daegu 41566, Republic of Korea

[7] Nano Lithography and Manufacturing Research Center, Korea Institute of Machinery and Materials (KIMM), Daejeon 34113, Republic of Korea

[8] Institute of Smart City and Intelligent Transportation, Southwest Jiaotong University, Chengdu 611756, China

[9] Department of Mechanical Engineering, KAIST, Daejeon 34141, Republic of Korea

Published online: 02 September 2026

ratios, intrinsic flexibility of individual nanoribbons, and aligned structural orientation into macroscopic fiber architectures, have attracted increasing attention [9–11]. Unfortunately, the practical utilization of the inorganic fibers has suffered from significant challenges, principally arising from their inherent low processability and pronounced brittleness [12, 13]. To address these limitations, several structural engineering strategies have been explored thus far, including polymer hybridization, hierarchical structural designs, and soft polymer encapsulation [14–16]. These strategies typically rely on composite or protective-layer formation but still face intrinsic constraints in achieving a high level of mechanical compliance required for ideal textile-integrated fibers [17].

This study strategically modulates the structural flexibility in inorganic fibers by reducing their thickness as described by the following relationship:

$$\varepsilon = h/2r_b, \tag{1}$$

where ε, h, and r_b represent maximum bending strain, material thickness, and bending radius of curvature, respectively [18]. Accordingly, decreasing the dimension of a material results in a proportional reduction of the maximum bending strain at a given radius of curvature. Since the maximum elongation at fracture is intrinsically governed by yield strength and Young's modulus, fiber thickness reduction presents a straightforward yet highly effective approach to minimize strain upon bending, significantly enhancing material flexibility [19]. Thus, despite the intrinsic brittleness of bulk inorganic materials, dramatically reducing their dimension to nanoscale provides substantial mechanical flexibility in the resulting nanoribbon structures, while retaining their original highly functional properties [20].

Based on the theoretical foundation described above, we demonstrate ultrasoft inorganic nanoyarns that unite material diversity, mechanical resilience, and multifunctional characteristics within a single textile-compatible structure (Fig. 1). Our inorganic nanoribbons, the basic units of our fiber, are precisely patterned by nanoimprint lithography (NIL) (Fig. 1a, b), offering excellent reproducibility and cost-effective scalability [21–24]. On the replicated polyurethane acrylate (PUA) mold, electron-beam evaporation is applied to selectively deposit various metals (Au, Ni, Pt) and metal oxides ($NiMn_2O_4$, $ZnMn_2O_4$) [25]. The deposition thickness is precisely controlled in the range of tens to hundreds of

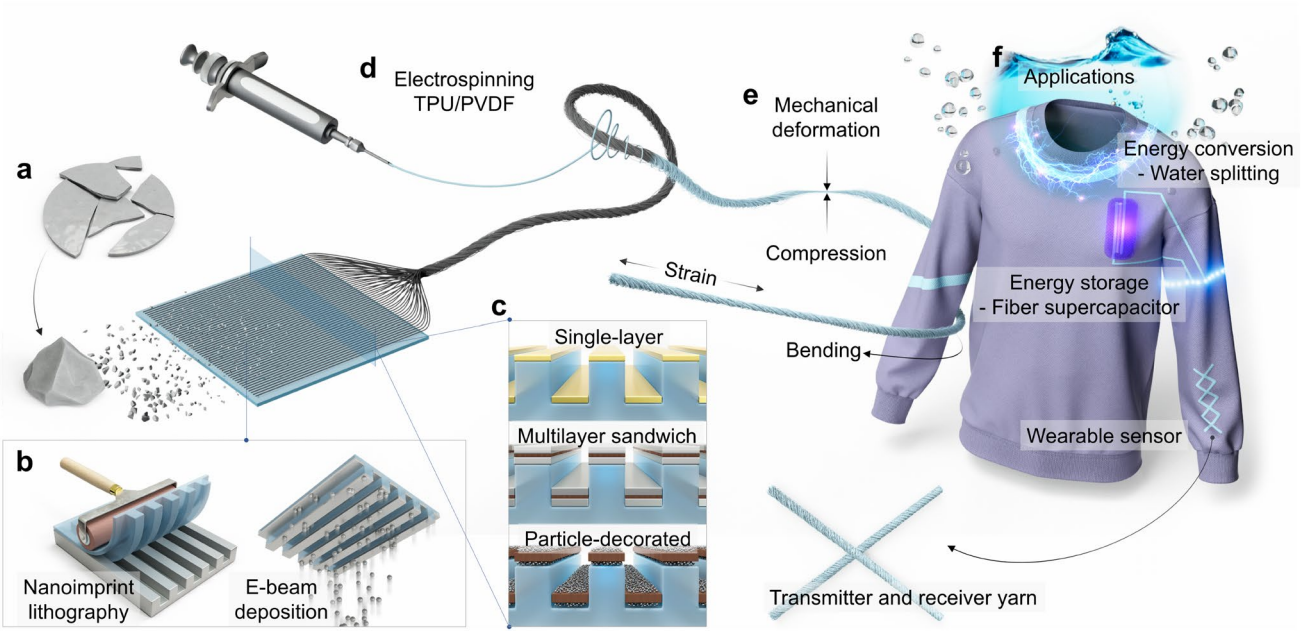


Fig. 1 Schematic illustration of the overall research concept and fabrication strategy for ultrasoft core–shell inorganic nanoyarns. Transformation of brittle inorganic materials into nanoribbons by reducing their thickness through **a** electron-beam evaporation process and **b** nanoimprint lithography. **c** Versatile deposition architectures achieved by tuning deposition conditions: single-layer, multilayer sandwich, and particle-decorated structures. **d** Formation of the core–shell nanoyarn via co-fabrication, in which plasma-assisted suspension and twisting of inorganic nanoribbons are combined with simultaneous electrospinning of polymer nanofibers. **e** Electromechanical stability of the core–shell nanoyarns under various deformation modes, including compression, bending, and stretching. **f** Integration of nanoyarns into textile matrices for multifunctional wearable platforms, including energy conversion, storage, and sensing applications

nanometers for diverse structures, including single-layer, multilayer sandwich, and particle-decorated configurations (Fig. 1c). These structures effectively compensate for the inherently low electrical conductivity of metal oxides, while enhancing the electrochemical reactivity of the inorganic nanoribbons. Simultaneously, an electrospinning process is applied to yield polymer nanofibers axially aligned along the inorganic core, subsequently constructing a uniform outer layer of hierarchical fiber structures to constitute core–shell architectures (Fig. 1d). Notably, the conductive core composed of metals or metal oxides can be electrically grounded, generating a localized electric field during electrospinning that guides and aligns the polymer jet toward the core surfaces. This co-fabrication strategy enhances the interfacial adhesion between the inorganic cores and the polymer shells, suppressing their aggregation and localized damage during deformation, thereby maintaining the structural stability and mechanical flexibility [26, 27].

Our core–shell nanoyarn synergistically combines the ultralow stiffness of individual nanoribbons with protective polymer shells, ensuring excellent electromechanical stability under repeated compression, bending, and tensile deformation, as well as variations in temperature and humidity (Fig. 1e). In addition, the yarn structure provides design flexibility in tailoring the geometry of inorganic devices, while offering a large effective surface area along the interconnected porous network [28]. Such a structural configuration maximizes the reactive surface area and facilitates electrolyte penetration and reactant diffusion, thereby greatly enhancing the electrochemical activity. In the representative utilization for water-splitting electrodes, the abundant active area and the efficient interfacial diffusion pathways improve the catalytic efficiency of the fiber structure. In fiber-type supercapacitors, the porous core–shell network and the pseudocapacitive behavior of Mn-based nanoribbons synergistically deliver high capacitance along with stable energy and power characteristics, while retaining excellent durability under long-term charge–discharge cycles as well as repeated bending. Finally, as a wearable mechanical force sensor, the core–shell nanoyarn reliably detects subtle mechanical stimuli, such as finger bending and light touch (Fig. 1f).

2 Results and Discussion

2.1 Fabrication and Structural Analysis of Core–Shell Inorganic Nanoyarns

Figure 2a illustrates the procedure for producing core–shell nanoyarn fibers. This manufacturing strategy relies on area-scalable unit processes and can be readily extended toward continuous large-area fabrication. First, (i) the polyurethane acrylate (PUA) solution is poured onto a silicon (Si) master with an 800 nm-wide nanoline pattern. A polyethylene terephthalate (PET) film, serving as the transparent support layer, is placed on top of PUA resin poured onto the Si master mold, followed by ultraviolet (UV) curing. After the UV curing process, using this nanoimprint mold, base metals and metal oxides are deposited onto the 800 nm nanoline pattern via electron-beam (e-beam) evaporation. While a single material can be used, multilayer deposition is also possible. After e-beam evaporation process, (ii) the metal or metal oxide deposited PUA mold is etched using oxygen-plasma treatment. As PUA is more susceptible to etching than metals or metal oxides, it is selectively removed first. To produce nanoyarns, the support layer must be completely etched so that the resulting metal/metal oxide nanoline structures can be detached and twisted. (iii) One end is fixed with tape, and the structure is mounted on a rotating device to twist the nanolines into yarns. (iv) To form a polymer shell, a ground is applied at both ends of the rotating device, and electrospinning is performed during rotation. This yields core–shell fibers with a metal or metal oxide nanoyarn core and a polymer shell.

Figure 2b–d show a cross-sectional scanning electron microscopy (SEM) and transmission electron microscopy (TEM) image of the nanoline PUA mold after various material depositions. Both single-layer and multilayer structures can be fabricated. For instance, a three-layer Ni–Pt–Ni nano-structure was successfully deposited. Figure 2b presents a focused ion beam-scanning electron microscopy (FIB–SEM) image of a nanoline-patterned mold coated with a single 100-nm Au layer. The Au film conformally covers the ridge surface of the 800-nm-wide line (highlighted in yellow). Additionally, compound deposition is feasible; a $MnZnO_3$–Ni–$MnZnO_3$ structure was also fabricated and analyzed using TEM (Fig. 2c-i). TEM elemental analysis using energy-dispersive X-ray spectroscopy (EDS) and depth profiling using X-ray photoelectron spectroscopy (XPS) confirmed that the composition and position of each layer matched the intended design. Cross-sectional elemental mapping further verified the layer-wise arrangement of Ni–Pt–Ni, and $MnZnO_3$–Ni–$MnZnO_3$ structures. In the Ni–Pt–Ni configuration, Ni layers of 40 nm thickness were observed flanking an 80 nm Pt layer. XPS depth profiling showed Ni-rich outer surfaces (46 at.%) transitioning to a Pt-dominant plateau at the center (51 at.%) and returning to Ni (22 at.%) (Fig. 2c-ii, S1a). The deposited thickness of multilayered nanoline pattern aligns with the nominal 40/80/40 nm design, confirming a symmetric Ni–Pt–Ni trilayer. In the $MnZnO_3$–Ni–$MnZnO_3$ structure (Fig. 2d-i), $MnZnO_3$ layers (170 nm) were positioned above and below a 100 nm Ni layer (Fig. S1b). In the $MnZnO_3$–Ni–$MnZnO_3$

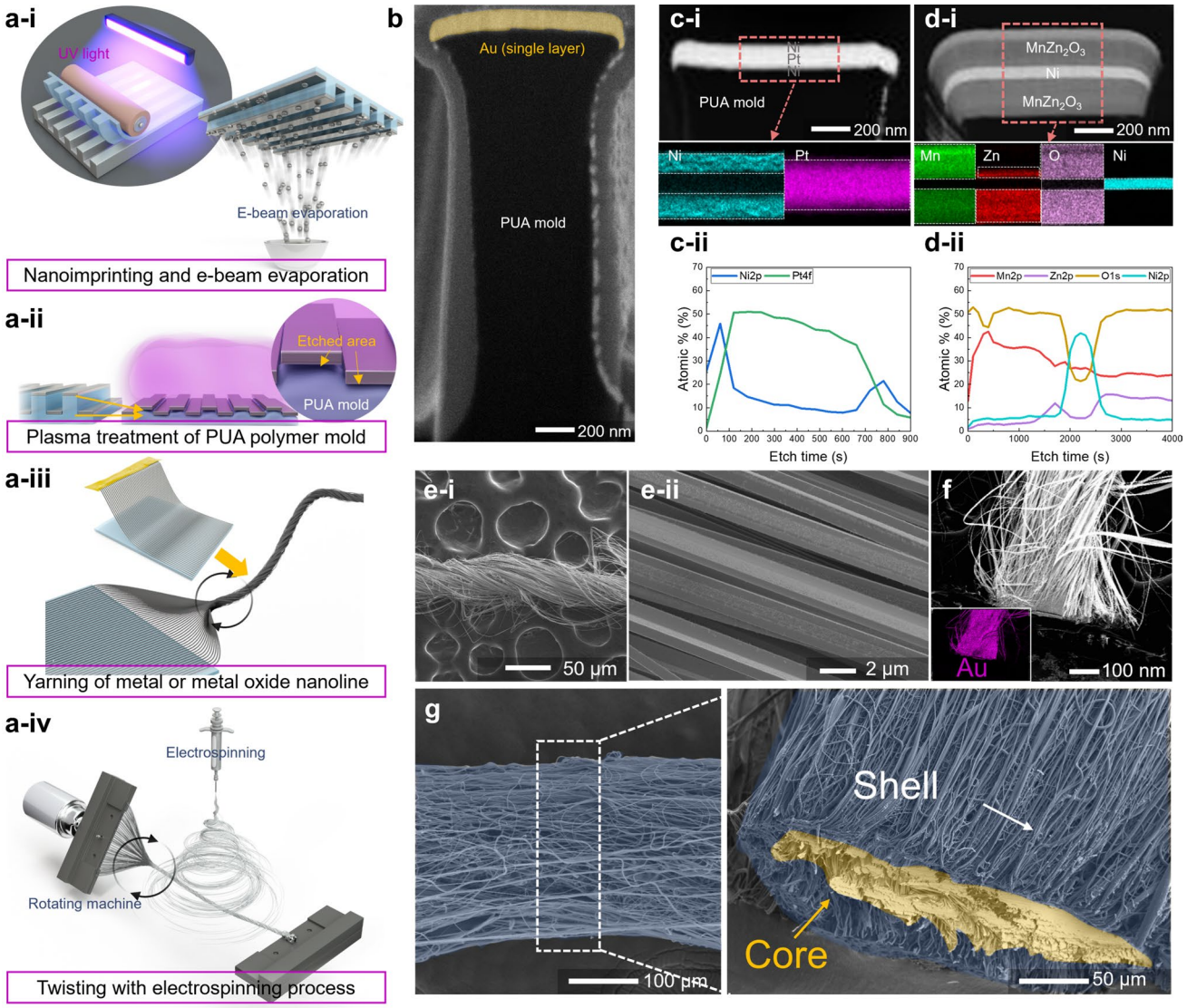


Fig. 2 Fabrication and characterization of core–shell inorganic nanoyarns. **a** Schematic of the process: nanoimprint replication of an 800-nm-pitch PUA nanoline mold, e-beam deposition of metals/metal oxides, selective oxygen-plasma removal of PUA to release the inorganic nanolines, mechanical twisting to form nanoyarns, and in situ electrospinning to create polymer-sheathed core–shell fibers. **b** FIB–SEM's cross section of a PUA ridge coated with a single 100 nm Au layer conformally covering the 800-nm-wide line (yellow). **c** (i) Cross-sectional TEM with EDS elemental maps for a Ni–Pt–Ni trilayer deposited on the PUA mold. (ii) XPS sputter-depth profile exhibiting Ni-rich outer regions transitioning to a Pt-dominant plateau, and returning to Ni, consistent with the 40/80/40 nm architecture. **d** (i) Cross-sectional TEM with EDS maps of a $MnZnO_3$–Ni–$MnZnO_3$ heterostructure. (ii) XPS depth profile showing oxide-rich plateaus bracketing a Ni-rich core, indicating sharp interfaces after plasma release. **e** SEM images of released nanolines and aligned bundles prior to twisting. **f** SEM of twisted Au nanoyarns; inset, Au EDS map confirming compositional purity. **g** SEM of a representative core–shell filament formed by electrospinning TPU onto rotating Au nanoyarns; fractured view highlights the Au (core) embedded within the electrospun TPU shell. Grounding of the conductive core orients the electrospun sheath along the interelectrode field

stack, the outer layers were oxide-rich with Mn + Zn + O totaling 85 at.%, which gave way to a Ni-rich core (43 at.%) at intermediate depths before returning to the oxide composition (Mn + Zn + O, 85 at.%) (Fig. 2d-ii).

These metal and metal oxide nanolines were twisted into yarns as shown in Fig. 2e. SEM imaging confirmed that the twisted Au nanoyarns maintained a uniform 800 nm width and consistent orientation. Figure 2f presents SEM and EDS results of the twisted Au nanoyarn cross sections, confirming the presence of Au through elemental mapping. The core–shell inorganic yarn cores consist of conductive metals or metal oxides, allowing electrical grounding. During twisting, in situ electrospinning directs the polymer jet to the grounded yarn, producing a dense, conformal sheath. The sheath orientation follows the electric field lines established by the grounded cores, yielding an aligned electrospun shell.

Figure 2g shows SEM images of core–shell structured yarns fabricated via electrospinning. In the top view, polymer fibers appear aligned along the electric field generated between both ends of the rotating device. These fibers are composed of electrospun thermoplastic polyurethane (TPU), with Au nanoyarns encapsulated as cores. As a representative result, a composite core–shell nanoyarn was fabricated with an Au nanoyarn core encapsulated by an electrospun TPU sheath. More broadly, the core can be engineered as single- or multilayer stacks of metals and metal oxides, while the shell can be tailored from a variety of electrospinnable polymers. As shown in Fig. S2, the electrospun fiber (shell) diameters range from 0.5 to 3.0 μm, with an average of 1.34 μm and a standard deviation of 0.57 μm. Figure S3 presents the Fourier-transform infrared (FTIR) spectra of electrospun TPU fibers containing Au nanoyarns, confirming the compositions of the polymer shell and metal core. Peaks corresponding to TPU (3330–3340 cm^{-1}: N–H stretching; 2940 cm^{-1}: C–H stretching; 1720–1730 cm^{-1}: C=O stretching; 1520–1530 cm^{-1}: N–H bending + C–N stretching) were observed, along with a 3400 cm^{-1} Au–OH peak formed on the nanowire surface during oxygen-plasma treatment.

2.2 Mechanical Flexibility and Electrical Stability of Core–Shell Nanoyarns

To evaluate the mechanical flexibility of the core–shell nanoyarn, the bending stiffness of both the core–shell nanoyarn and the Au core yarn was determined, and the relative contributions of each component to the overall stiffness were quantitatively analyzed. A three-point bending test with fixed supports was conducted (Fig. 3a, inset). Central load P (N) and central deflection δ (mm) were measured, and bending stiffness ($E_{\text{effective}}I$) was subsequently calculated from the load–deflection relationship as:

$$\left(E_{\text{effective}}I\right) = PL^3/192\delta, \tag{2}$$

where $E_{\text{effective}}$ is the effective Young's modulus, I is the second moment of area about the neutral axis, and L is the span length (mm). The bending stiffness of the Au core yarn was calculated to be $(E_{\text{effective}}I)_{\text{Au core yarn}} = 0.208$ N·mm^2, whereas that of the core–shell nanoyarn was calculated as $(E_{\text{effective}}I)_{\text{core–shell nanoyarn}} = 0.238$ N·mm^2, corresponding to a 14.4% increase. Contribution analysis revealed that the Au core accounted for 87.4% of the total bending stiffness. The contribution of the TPU shell is represented by the term E_sI_s, where E_s is the Young's modulus of the electrospun TPU shell ($E_s = 17.1$ MPa), and I_s is the second moment of area of the TPU shell about the neutral axis [29]. The product E_sI_s was calculated to be 0.00513 N·mm^2, accounting for 2.2% of the total bending stiffness. This small contribution results from the pronounced difference between the Young's modulus of the TPU shell and the effective Young's modulus of the Au core yarn ($E_c = 3.12$ GPa, Supplementary Note). The remaining contribution arises from interfacial shear-coupling at the Au–TPU interface, which is mediated by van der Waals interactions. This interfacial contribution can be described as a shear term in the effective bending stiffness of fiber-bundle-based structures and has often been overlooked in conventional fiber systems [30, 31]. Accordingly, in this study, the effect was quantitatively identified by incorporating it into the overall bending stiffness together with the other component contributions as expressed in the following equation:

$$\begin{aligned}\left(E_{\text{effective}}I\right)_{\text{core - shell nanoyarn}} = &\left(\left(E_{\text{effective}}I\right)_{\text{Au core yarn}}\right) \\ &+ \left(E_sI_s\right) + \eta E_cA_c\left(r_m\right)^2,\end{aligned} \tag{3}$$

where η is the interfacial shear-coupling coefficient, A_c is the cross-sectional area of the core, and r_m is the lever arm, which represents the effective distance for shear transfer from the core to the shell. The interfacial shear-coupling term was calculated to be 0.02487 N·mm^2, corresponding to 10.4% of the total bending stiffness of the core–shell nanoyarn.

A comparison with diverse yarn materials, including conductive polymer fibers, common textile fibers, carbon-based conductors, metal wires, and high-strength fibers, is presented in Fig. 3b, c and Table S1. The effective Young's modulus of the core–shell nanoyarn (0.65 GPa) was lower than that of a representative textile fiber, nylon (about 2.5 GPa), and approached that of high-performance polymer materials such as Teflon (about 0.5 GPa), thereby confirming its superior flexibility. In addition, the electrical conductivity of the core–shell nanoyarn reached 2.16×10^6 S/m (Fig. S4a), higher than that of hybrid stainless-steel–cotton yarns (about 5.0×10^5 S/m), while exhibiting a bending stiffness about four times lower (0.95 N·mm^2 for the hybrid-SS yarns). Moreover, the electrical conductivities obtained from five independently fabricated samples exhibited a relative standard deviation (RSD) of 10.03%, indicating reliable fabrication reproducibility of the core–shell nanoyarn (Fig. S4b). These results demonstrate that the core–shell nanoyarn simultaneously secures high flexibility, electrical conductivity, and reliable fabrication reproducibility beyond those of conventional fibers and textile electrodes. Its architecture, in which both the core and the shell are designed as nanoscale structural units, forms a nanoporous network that provides a large specific surface area and enhanced electrochemical reactivity, while also allowing broad material diversity as the compositions of the inorganic core (e.g., Au, Pt, Ni, $NiMn_2O_4$, and $ZnMn_2O_4$) and the polymeric shell (e.g., TPU, poly(vinylidene fluoride) (PVDF)) can be readily tailored to impart specific functionalities. Taken together,

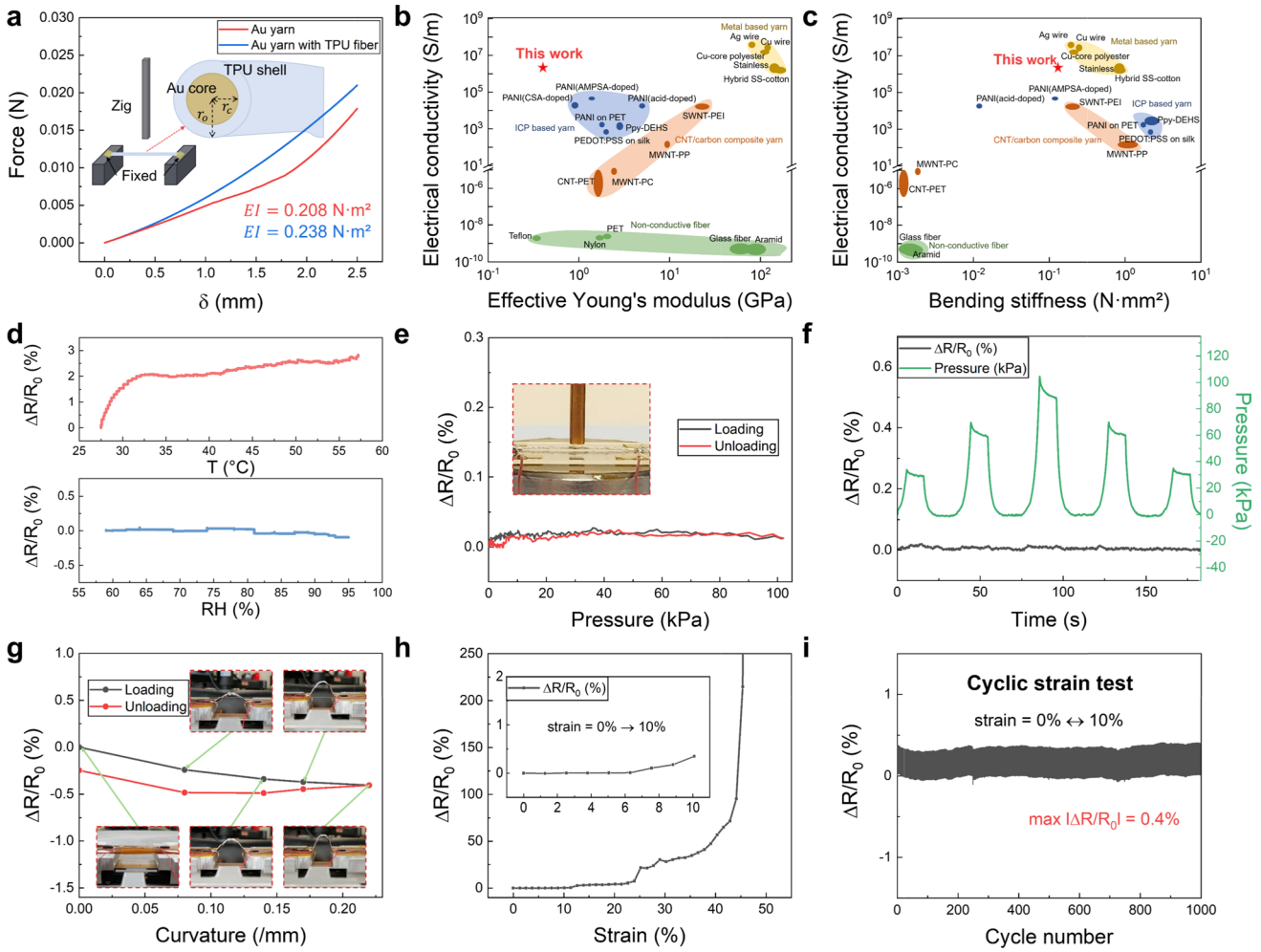


Fig. 3 Mechanical and electrical characterization of the core–shell nanoyarn. **a** Schematic illustration of the three-point bending test for the core–shell nanoyarn and the corresponding calculated bending stiffness. Comparison of various yarn materials: **b** effective Young's modulus vs. electrical conductivity, **c** bending stiffness vs. electrical conductivity. **d** Environmental stability confirmed by relative electrical resistance change under temperature (27–57 °C) and relative humidity (60%–95% RH) variations. **e** Relative resistance change response during loading–unloading under 0–100 kPa compression. **f** Dynamic compression cycles within the same pressure range. **g** Optical images of nanoyarns bent up to a curvature of 0.215 mm^{-1} and corresponding relative resistance change during loading–unloading. **h** Relationship between tensile strain and relative resistance change up to 45%, confirming electrical stability within 10% strain. **i** Relative resistance change during 1000 tensile cycles in the 0–10% strain range

these attributes highlight that the dual strategy of reducing the thickness of inorganic components and introducing the shell as an insulating layer provides an effective and versatile route toward the realization of high-performance fiber electrodes.

For wearable applications, the core–shell nanoyarn maintains electrical stability under various environmental and mechanical stimuli [32]. Accordingly, environmental stability was examined by measuring the relative electrical resistance change under variations in temperature and humidity (Fig. 3d). Under temperature variation, the relative resistance change of the core–shell nanoyarn increased sharply between 27 and 33 °C, followed by a gradual plateau from 33 to 57 °C, with an overall variation of about 2.8%. This behavior contrasts with the intrinsic property of Au, in which resistance typically increases linearly with rising temperature [33]. The distinct temperature dependence observed in the core–shell nanoyarn arises from structural and interfacial effects as thermal expansion or softening of the polymer shell enhances interfacial contact upon heating [34]. This compensatory mechanism offsets the intrinsic positive temperature coefficient of resistance (TCR) of Au, leading to the observed plateau beyond 33 °C. The relative resistance change under relative humidity (RH) conditions of 60%–95% remained within (±0.03)%. Such stability in resistance is attributed to the chemical inertness of Au,

indicating that the electrical performance of the core–shell nanoyarn is virtually unaffected by humidity.

Electromechanical stability was evaluated under compressive, bending, and tensile conditions. Under static pressure loading–unloading cycles (0–100 kPa), the relative electrical resistance change was maintained below 0.03% (Fig. 3e). Likewise, dynamic cyclic compression within the same range produced negligible resistance variation (Fig. 3f). To further verify long-term durability under repeated compressive deformation, the core–shell nanoyarn was subjected to 1000 pressure loading–unloading cycles from 0 to 100 kPa. The relative resistance change remained below 0.21% even after 1000 cycles (Fig. S5a), confirming the excellent resistance stability of the core–shell nanoyarn under repeated high-pressure deformation. Figure 3g illustrates the core–shell nanoyarn bent to a curvature of up to 0.215 mm^{-1}, demonstrating its flexibility; the relative resistance change remained below 0.3% across this curvature range. In addition, no significant changes were observed under dynamic bending or after 1000 bending cycles (Fig. S5b, c). In tensile tests, the relative resistance change was stable (< 0.5%) up to 10% strain. However, a modest increase of about 7.5% was observed at 25% strain, followed by a sharp rise to 21.6% (Fig. 3h). The high stability within 0–10% strain is attributed to pre-compression of approximately 10% introduced during core–shell nanoyarn twisting, which acted as a mechanical buffer. Moreover, the elastomeric TPU shell distributed the applied stress uniformly, preventing localized stress concentration within the nanoribbon core [35]. As a result, this feature suppressed premature breakage of conductive paths, thereby maintaining a robust percolation network. After dynamic stretching or 1000 tensile loading–unloading cycles, the relative resistance change remained within 0.4% (Fig. 3i, S5d). To further validate the structural design tolerance of the core–shell nanoyarn, the effects of nanoyarn length, shell thickness, and core diameter on resistance stability were systematically examined under pressure, bending, and tensile deformation. As shown in Fig. S6, Au–TPU nanoyarns with lengths of 1, 3, and 5 cm maintained low-resistance variations under pressure and bending, while preserving stable electrical responses up to 10% strain under tensile deformation. This geometry-tolerant stability was also observed in nanoyarns with different shell thicknesses and core diameters, confirming that the electromechanical robustness of the Au–TPU nanoyarn is not limited to a single structural dimension. Collectively, these results demonstrate that the core and the shell act cooperatively to dissipate mechanical energy and preserve conductive pathways, supporting reliable long-term operation in wearable sensors and flexible electronic devices.

2.3 Performance Benchmarking and Cycling Stability of Pt/Ni–TPU Nanoyarn Electrodes for Energy Conversion

Pt/Ni nanoyarn electrodes exhibit efficient oxygen evolution reaction (OER) activity in alkaline media, arising from the synergistic catalytic effects of Pt and Ni combined with the high surface area and mechanical flexibility of the yarn structure (Fig. 4a). The electrochemical OER performance was evaluated using a standard three-electrode configuration in 1 mol/L KOH, where the Pt/Ni–TPU core–shell nanoyarn was directly employed as the working electrode, with Pt and Hg/HgO serving as the counter and reference electrodes, respectively. The polarization curves of Pt/Ni nanoyarn electrodes without and with the TPU shell are presented in Fig. 4b, c, respectively, including their evolution after 1000 cycles. In the first cycle, the catalytic activity follows the order Pt/Ni–TPU < Pt/Ni, with overpotentials (η) of 327.1 and 282.1 mV, respectively, at 10 mA/cm^2. Although the TPU shell is electrochemically active, its insulating nature may initially hinder reactant transport and electrode wetting, thereby lowering the performance of Pt/Ni–TPU compared to bare Pt/Ni. Interestingly, after 1000 cycles, this trend is reversed: while the Pt/Ni yarn exhibits significant activity loss ($\eta = 451.4$ mV), the Pt/Ni–TPU nanoyarn shows enhanced efficiency ($\eta = 251.2$ mV). This behavior highlights the protective role of the TPU shell in suppressing structural deterioration during extended cycling, while progressively allowing reactant migration through the polymer barrier through extent cycling (Fig. 4d).

To further investigate the catalytic kinetics, Tafel plots were constructed for the yarn electrodes. The Pt/Ni nanoyarn, which initially showed a slope of 72.8 mV/dec, deteriorated to 274.3 mV/dec after 1000 cycles, consistent with the corrosion-prone nature of Pt–Ni electrodes in alkaline media (Fig. 4e). The Pt/Ni–TPU nanoyarn exhibited slopes of 84.6 and 64.2 mV/dec at cycle 1 and cycle 1000, respectively, indicating improved reaction kinetics upon prolonged cycling (Fig. 4f).

The time-evolution electrochemical impedance spectroscopy (EIS) spectra reveal distinct impedance evolution behaviors for the Pt/Ni and Pt/Ni–TPU yarn electrodes. The bare Pt/Ni yarn exhibits a less stable and more irregular impedance response during cycling, suggesting progressive interfacial instability under OER conditions (Fig. 4g). This behavior may be associated either with catalyst detachment, surface reconstruction/oxidation, or deterioration of electrical contact during prolonged electrochemical operation [36].

In contrast, the Pt/Ni–TPU yarn shows a gradual decrease in semicircle diameter with increasing cycle number, indicating a reduction in interfacial charge-transfer resistance

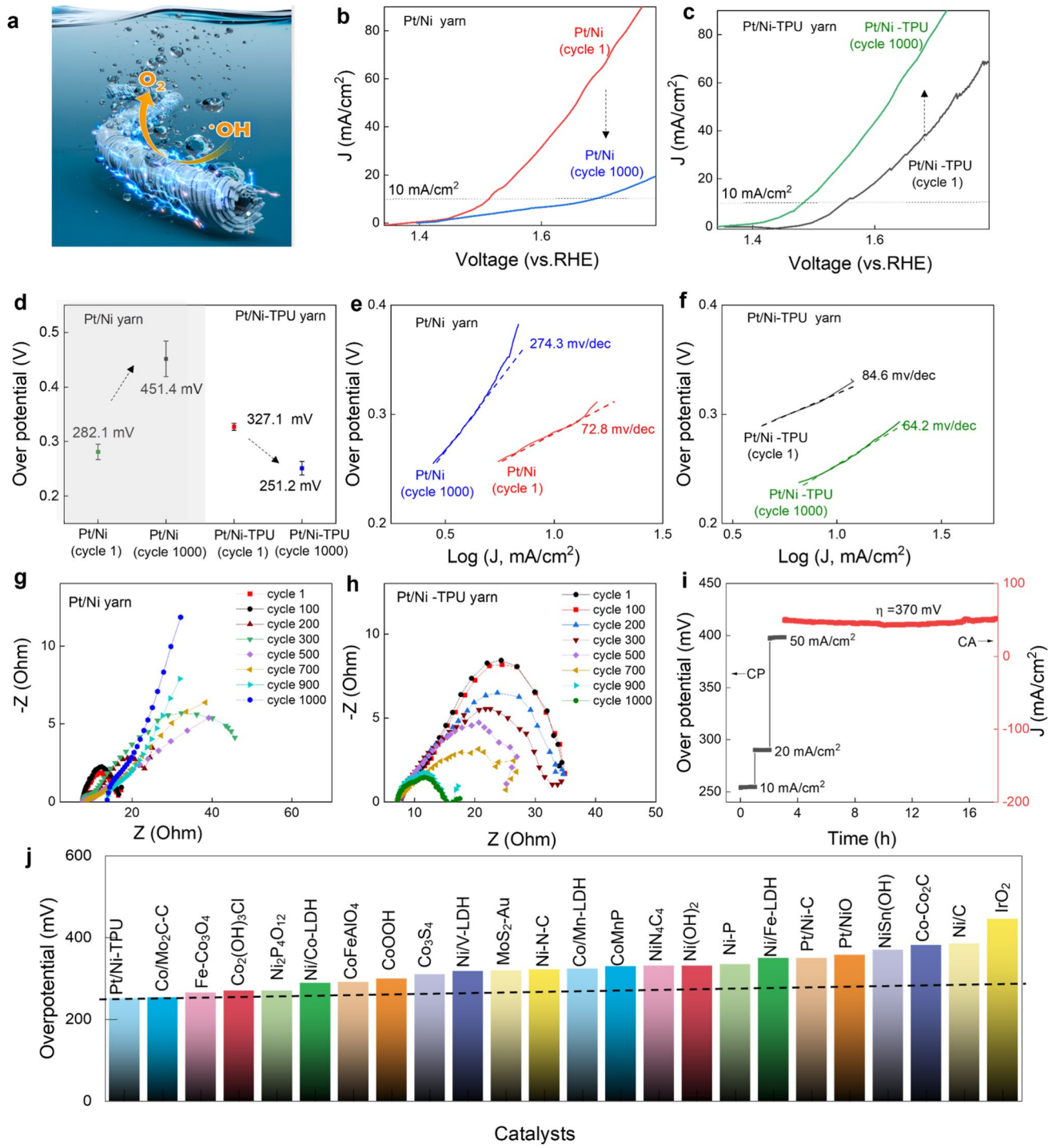


Fig. 4 Electrocatalytic performance of Pt/Ni nanoyarn electrodes with and without TPU shells in alkaline OER. **a** Schematic illustration of the Pt/Ni–TPU core–shell nanoyarn electrode. Polarization curves of **b** Pt/Ni and **c** Pt/Ni–TPU nanoyarn electrodes at cycle 1 and after 1000 cycles. **d** Overpotential at a current density of 10 mA/cm^2 recorded over 1000 cycles for both Pt/Ni and Pt/Ni–TPU yarn electrodes. Tafel plots for **e** Pt/Ni and **f** Pt/Ni–TPU before and after cycling. Nyquist plots showing the evolution of the interfacial charge-transfer characteristics for **g** Pt/Ni and **h** Pt/Ni–TPU electrodes during cycling. **i** Durability tests including sequential CP (10, 20, 50 mA/cm^2 over 6 h) and CA (20 h), confirming excellent long-term catalytic stability. **j** Benchmark comparison of OER overpotentials at 10 mA/cm^2 for the Pt/Ni–TPU nanoyarn electrode and representative state-of-the-art OER catalysts reported in the literature. The horizontal dashed line denotes the overpotential of the Pt/Ni–TPU nanoyarn electrode, highlighting its competitive or superior electrocatalytic performance

(Fig. 4h). This behavior is consistent with progressive electrolyte infiltration through the TPU shell and gradual activation of the Pt/Ni core. Consequently, the initially lower activity of the Pt/Ni–TPU electrode can be attributed to delayed electrolyte wetting and restricted ion transport caused by the polymer shell.

As cycling proceeds, electrolyte penetration improves the accessibility of electrochemically active sites, while the TPU shell simultaneously serves as a mechanically compliant protective framework that helps preserve the structural integrity of the electrode. As a result, the Pt/Ni–TPU yarn exhibits enhanced long-term electrochemical stability and ultimately surpasses the performance of the bare Pt/Ni yarn after 1000 cycles.

Furthermore, the Pt/Ni–TPU nanoyarn electrode retained its high catalytic activity during durability testing (Fig. 4i). A sequential chronopotentiometry (CP) test at current densities of 10, 20, and 50 mA/cm^2 over 6 h revealed that the overpotentials gradually increased from 253.6 to 398.4 mV while maintaining stable operation at each step. In addition, a continuous chronoamperometry (CA) test up to 20 h confirmed excellent stability, with the electrode sustaining an average current density of 53.5 mA/cm^2 at an overpotential of 370 mV. These results demonstrate the superior durability and long-term catalytic efficiency of the Pt/Ni–TPU nanoyarn electrode under alkaline OER conditions. A benchmarking comparison of overpotentials with previously reported high-performance OER catalysts is summarized in Fig. 4j, demonstrating that the Pt/Ni–TPU nanoyarn electrode performs comparably or even superior to state-of-the-art electrocatalysts [37–41]. A more detailed comparison is provided in Table S2.

2.4 Electrochemical Energy Storage Performance of Core–Shell Fiber Supercapacitors

The porous architecture and high redox activity of $ZnMn_2O_4$ (ZM) and $NiMn_2O_4$ (NM) nanoyarns facilitate efficient electrolyte diffusion and electron transport, thereby endowing them with excellent energy storage potential. To demonstrate their applicability in flexible fiber supercapacitors (FSCs), we fabricated asymmetric yarn devices by pairing nanoyarns with carbon nanotube (CNT) yarns and a poly(vinyl alcohol) (PVA)/KOH gel electrolyte (Fig. 5a inset, S7). The PVA/KOH gel electrolyte was infiltrated into the yarns under vacuum, ensuring penetration through the TPU shell and effective wetting of the nanoribbon cores (Methods).

Electrochemical performance was evaluated within a voltage window of − 0.8 to 0.8 V (1.6 V). The cyclic voltammetry (CV) curves of ZM and NM nanoyarns (Fig. 5a, b) exhibit non-rectangular profiles, characteristic of pseudocapacitive redox processes. Consistently, galvanostatic charge–discharge (GCD) profiles display nonlinear and asymmetric triangular shapes (Fig. 5c, d), indicative of battery-like faradaic contributions. The rapid voltage drop at higher potentials, followed by extended discharge plateaus at lower potentials, suggests potential-dependent variations in ionic diffusion kinetics, charge-transfer rates, and reaction mechanisms, typical of battery like materials. Importantly, the TPU encapsulation layer exerts negligible influence on capacitance (Fig. S8).

From the GCD data, the areal and volumetric specific capacitances of ZM and NM nanoyarn electrodes were determined (Fig. 5e, f). ZM and NM exhibit areal capacitances of 1.51 and 1.32 F/cm^2 at current densities of 1.5 and 2.0 mA/cm^2, respectively, which are comparable to or higher than those of state-of-the-art fiber supercapacitors [42–45]. The corresponding volumetric capacitances reach 303.4 and 238.1 F/cm^3, highlighting their high charge-storage efficiency in confined geometries. The devices also display exceptional durability and mechanical resilience. Both ZM and NM nanoyarn FSCs retain approximately 99.5% of their capacitance after 20000 charge–discharge cycles (Fig. 5g, h). Nearly 100% of the initial capacitance is preserved even under bending to 180° (Fig. S9), and negligible capacitance loss is observed after 1000 repeated bending (90°) and straightening (180°) cycles. Statistical analysis further confirms that areal capacitances remain highly stable for both systems under mechanical deformation (Fig. S10).

Energy and power densities were calculated at different current densities (Fig. S11, S12). Interestingly, both ZM and NM nanoyarn devices exhibit nearly constant energy and power densities across the tested current ranges, reflecting their dominant supercapacitive behavior. The maximum volumetric energy densities of 107.8 and 84.6 mWh/cm^3, and the corresponding power densities of 0.76 and 0.83 W/cm^3, for ZM and NM respectively, significantly outperform many previously reported FSCs (Fig. 5i, Table S3).

2.5 Smart Textile Implementation of Core–Shell Nanoyarn Wearable Sensors

To validate the applicability of the developed core–shell nanoyarn for smart textiles, it was integrated into actual garments and further implemented as a wearable sensor system [46–48]. Figure 6a-i shows commercial Cu wires, Au yarns, and core–shell nanoyarns embedded within commercial knitted fabrics. After repeated bending and straightening of the arm, the commercial Cu wire exhibited plastic deformation due to its limited flexibility. Moreover, the Au yarn experienced cracking and fracturing due to the mechanical fragility of the Au nanoribbons and aggregation within its nanostructure. In contrast, the core–shell nanoyarn maintained excellent conformability and structural stability within the knitted substrate (Fig. 6a-ii). This robustness arises from the intrinsic mechanical mechanism of fiber systems, in which the aligned, twisted core–shell architecture redistributes

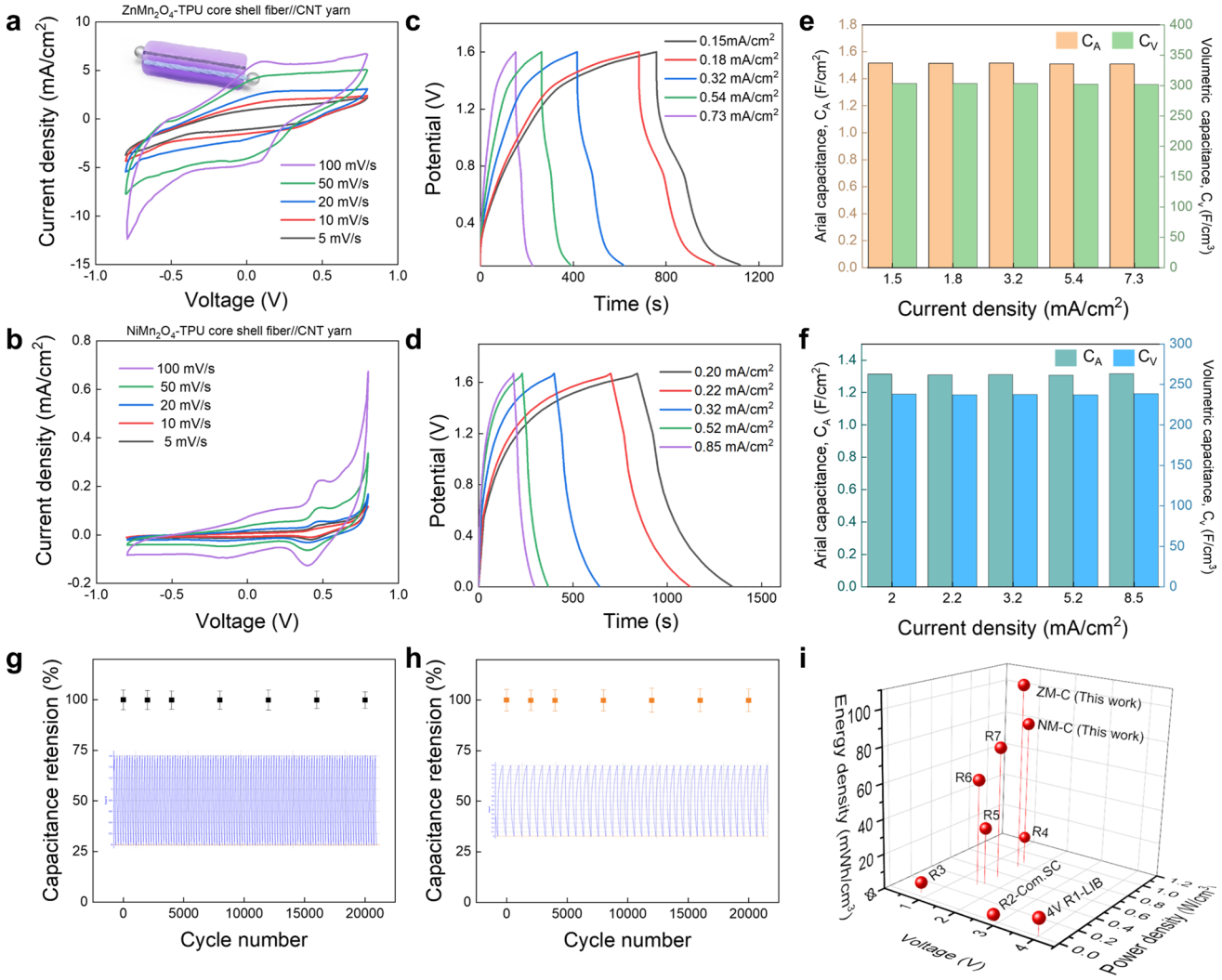


Fig. 5 Electrochemical performance of $ZnMn_2O_4$ (ZM) and $NiMn_2O_4$ (NM) nanoyarn-based fiber supercapacitors (FSCs). **a**, **b** Cyclic voltammetry curves of ZM and NM nanoyarn electrodes, showing non-rectangular profiles characteristic of pseudocapacitive redox activity. **c**, **d** Galvanostatic charge–discharge (GCD) curves displaying non-linear triangular shapes with voltage plateaus, indicative of faradaic contributions. **e**, **f** Areal and volumetric specific capacitances derived from GCD, with ZM and NM, respectively. **g**, **h** Long-term cycling stability demonstrating approximately 99.5% capacitance retention after 20000 charge–discharge cycles for ZM and NM, respectively. **i** Energy and power densities comparison of FSCs with many previously reported FSCs including commercial supercapacitor and 4 V Lithium-ion battery

tensile and bending stresses along a helical pathway, thereby delaying structural failure. Two fiber supercapacitors (ZM and NM) were then connected in series and sewn into a sweater to power a 3 V flexible light-emitting diode (LED) (Fig. 6b). Continuous illumination was maintained for several minutes even under repeated bending and stretching (Fig. S13, Supplementary Movie). These results demonstrate that the core–shell nanoyarn provides outstanding mechanical flexibility, robustness, and practical applicability without restricting the wearer's movement.

The wearable sensor was constructed with two crossed electrodes, in which the TPU shell acted as the dielectric layer. Upon compression of the nanoyarn, the TPU shell deformed and the distance between the Au core yarns decreased, resulting in a change in capacitance. The fabricated sensor was capable of detecting subtle forces within 0.36 N, corresponding to the range of daily human activities (Fig. S14). To evaluate its performance, the core–shell nanoyarn was integrated into a glove, and relative capacitance changes were recorded at finger bending angles of 30°, 60°, and 90°, with a maximum increase of 2.7% observed at 90° (Fig. 6c). In addition, relative capacitance variations were measured under finger touches with different forces and speeds. The calibration results clearly reflected the differences in applied loads between light and strong touches,

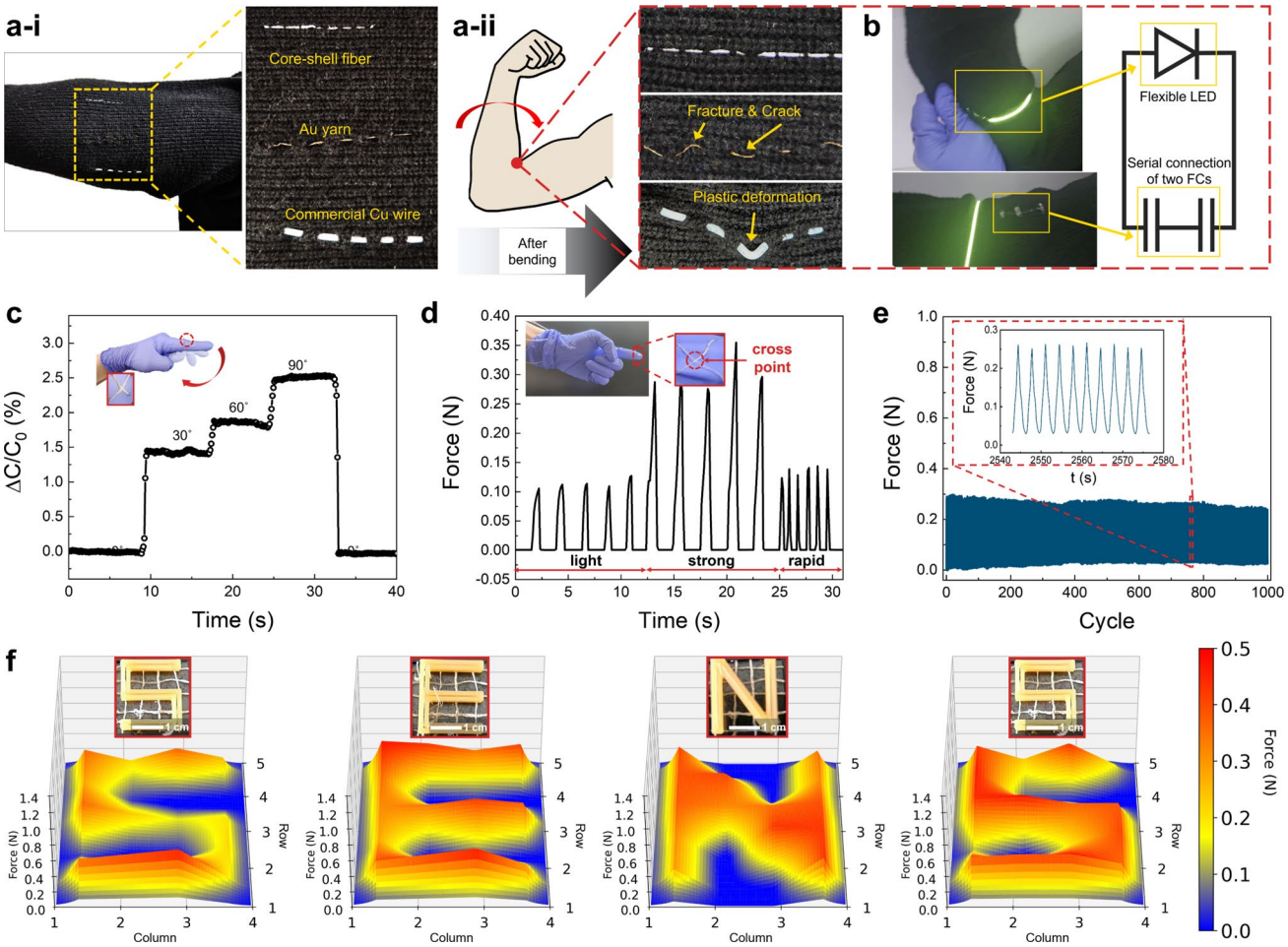


Fig. 6 Smart textile implementation of core–shell nanoyarn wearable sensors. **a** (i) Integration of commercial Cu wire, (ii) Au yarn, and core–shell nanoyarn into knitted fabrics, showing superior conformability of the nanoyarn after repeated arm bending. **b** Two fiber-type supercapacitors (ZM/CNT) connected in series and integrated into a knitted sweater to power a 3 V flexible LED. Continuous and stable illumination was maintained even during repeated bending and stretching. **c** Relative capacitance changes under finger bending at different angles. **d** Calibration results of the sensor under finger touches with different forces and speeds. **e** Long-term durability over 1000 repeated loading cycles. **f** A 5×4 sensor array precisely monitored the magnitude and spatial distribution of applied forces and distinctly reproduced the shapes of 3D-printed letter stamps "S," "E," "N," and "S."

while stable and consistent signals were maintained under fast touches regardless of speed (Fig. 6d). The dynamic response characteristics were further evaluated under an applied load of 0.3 N. As shown in Fig. S15, the sensor exhibited a response time of 92 ms and a recovery time of 87 ms, demonstrating its ability to rapidly and reversibly transduce transient mechanical stimuli into capacitive signals. Notably, after 1000 repetitive cycles at an applied load of 0.3 N, the sensor exhibited negligible performance degradation, demonstrating excellent durability (Fig. 6e). In addition, the sensor was tested under water exposure (Fig. S16). Relative capacitance rapidly saturated at about 310%, exceeding the range of typical force responses, but fully returned to baseline after 24 h of drying.

Finally, a 5×4 sensor array was fabricated to monitor both the magnitude and distribution of pressure (Fig. 6f). This array utilized a mutual capacitance measurement system, where each intersection between transmitter and receiver yarn acted as an individual sensing element. The acquired data were reconstructed using a regular-grid interpolation algorithm to visualize the continuous pressure distribution. When 3D-printed stamps with letters, such as "S," "E," and "N", were applied onto the sensor array, the measured responses distinctly reproduced the corresponding letter shapes, validating the platform's spatial resolution. These results demonstrate that the core–shell nanoyarn serves as a highly reliable sensing platform for smart textiles and precise human–machine interfaces.

3 Conclusions

This study has demonstrated the successful fabrication of ultrasoft core–shell nanoyarns through sequential processes, including plasma-assisted nanoribbon suspension, mechanical twisting, and electrospinning. The synergistic integration of nanoribbon twisting with electric-field-guided electrospinning enables the highly reproducible formation of core–shell architectures. The proposed architecture simultaneously achieves high flexibility, electrical conductivity, long-term stability, and strong performance across diverse applications, including water-splitting electrodes, fiber-type supercapacitors, and wearable sensors. In particular, the excellent cycling stability of the Pt/Ni–TPU nanoyarn electrode during prolonged oxygen evolution reaction operation and the high volumetric energy-storage performance of the core–shell fiber supercapacitor demonstrate that this architecture offers performance advantages over simple conductive fiber configurations. Collectively, these findings establish core–shell nanoyarns as a promising platform capable of unifying energy conversion, energy storage, and sensing functions in next-generation smart textiles. Nevertheless, several critical challenges remain before this inorganic fiber architecture can be implemented in real-world applications. A key priority is extending the yarn length, which is currently limited to relatively short segments of about 9 cm. In this regard, a continuous roll-to-roll nanoimprinting process is strongly needed and expected to enable large-area mold replication and continuous yarn production. Such a process would significantly enhance scalability and manufacturing throughput, paving the way toward industrial-scale implementation.

In addition, further advances in material design are required to broaden electrochemical applicability. For example, in water-splitting applications, integrated multi-composition designs for neutral or acidic electrolyte conditions would be desirable. In supercapacitors, optimizing the electrode–electrolyte interfaces would further improve charge storage at high current densities. For wearable sensors, scaling toward multi-channel arrays, multimodal signal detection, including pressure, temperature, and humidity, and machine learning assisted signal analysis would be essential for realizing intelligent sensing systems. Beyond the demonstrated material systems, the independent tunability of the inorganic core and polymer shell provides an additional pathway for expanding the function of this platform. For example, electrochromic transition-metal oxide cores, such as WO_3 and NiO, could be incorporated to realize fiber-type electrochromic sensors or textile-integrated color-changing displays. Semiconducting metal oxide cores, such as SnO_2, WO_3, In_2O_3, and CuO, could also be explored for wearable multi-gas sensing fibers, potentially enabling the detection of gasses, such as NO_2, NH_3, H_2S, CO, and VOCs, through material-dependent surface reactions. In addition, metal oxide cores such as ZnO or MnO could be used as fiber-type anode materials for wearable batteries, where the nanoyarn geometry may provide mechanical deformability while maintaining electrochemical functionality. In addition, replacing the TPU shell with a functional polymer shell such as PVDF could introduce dielectric or piezoelectric functionality, enabling capacitive sensors, self-powered pressure sensors, or piezoelectric energy harvesting fibers.

Nevertheless, the ultrasoft core–shell nanoyarns developed in this study represent an important step forward in the technological field of smart textiles. By synergistically combining the desirable electrical and chemical functionalities of inorganic nanoribbons with the genuine mechanical compliance of polymer shells, this platform overcomes the limitations of traditional yarn materials. The demonstrated versatility across catalytic, energy storage, and wearable sensing applications underscores its transformative potential. Along with continued progress in scalable manufacturing and material optimization, this platform could evolve into a foundational technology for intelligent wearable systems, enabling stable and adaptive operation in highly dynamic real-world environments.

4 Experimental Section

4.1 Electromechanical Characterization

The electromechanical behavior of the Au–TPU core–shell nanoyarns was systematically evaluated under bending, compression, and tensile conditions. The bending stiffness was quantified using a fixed-support three-point bending configuration. A universal testing machine (UTM, AGS-X, Shimadzu, Japan) equipped with a 3 mm × 3 mm load cell applied a central load to the suspended yarn, which was fixed at both ends with copper tape. The effective bending stiffness was determined from the linear elastic region of the load–deflection curve. The electrical resistance was simultaneously monitored using a source meter (Keithley 24xx Series, Tektronix, USA). Both ends of the nanoyarn were electrically connected to copper wires with silver paste to minimize contact resistance. For the compression test, the nanoyarn was mounted on a flat glass slide and loaded up to 0.36 N using the same UTM setup. Tensile and cyclic bending tests were performed using a precision linear stage (HR45-SSP, Hanshin Robot Co., Republic of Korea) under programmable displacement control. For bending tests, the nanoyarn was integrated onto a flexible PET film to maintain stable curvature, while both ends were secured with polyimide (PI) adhesive tape.

Environmental stability was evaluated by monitoring real-time resistance variations under varying temperature and humidity. A DHT-11 temperature–humidity sensor module was interfaced with an Arduino Mega 2560 board for continuous data acquisition. The environment was controlled inside a fume hood using a hotplate for temperature regulation and a commercial humidifier for humidity adjustment.

4.2 Electrochemical Water-Splitting Experiments

The electrocatalytic performance of the synthesized Pt/Ni–TPU core–shell nanoyarns toward water-splitting was systematically investigated in 1.0 mol/L KOH aqueous electrolyte using a conventional three-electrode configuration. A Hg/HgO electrode and a platinum wire were employed as the reference and counter electrodes, respectively, while the prepared Pt/Ni–TPU nanoyarn was directly used as the working electrode. Each nanoyarn electrode was fixed on a PET substrate using Ag paste to ensure reliable electrical contact and mechanical stability during measurement. The active mass of each electrode was accurately measured prior to every experiment.

Electrochemical measurements were carried out using a Bio-Logic SAS SP-200 electrochemical workstation. Cyclic voltammetry (CV) and linear sweep voltammetry (LSV) were performed at various scan rates and potential ranges to evaluate catalytic activity and reaction kinetics. The corresponding Tafel slopes were derived from the polarization curves to estimate the intrinsic kinetics of the oxygen evolution reaction (OER). Chronopotentiometric (CP) and chronoamperometric (CA) measurements were conducted to assess the long-term durability and operational stability under continuous OER conditions. EIS was recorded to monitor changes in charge-transfer resistance.

4.3 Fabrication of Solid-State Supercapacitors

All-solid-state supercapacitors were assembled by integrating transition metal oxide (TMO) core–shell nanoyarns with CNT yarns on flexible PET films or fabric substrates. The yarn electrodes were aligned in a parallel configuration and fixed using double-sided Cu tape, securing one end of each yarn to the substrate. Electrical contact was established by coating Ag paste on the same end. Subsequently, a PVA/KOH polymer gel electrolyte was uniformly applied to the yarns using a fine brush, and the assembled device was dried under vacuum for 30–60 min. Both the positive and negative electrodes were precharged and mass-balanced to ensure optimal electrochemical performance.

Electrochemical measurements (CV, GCD, and EIS) were carried out using a Bio-Logic SAS SP-200 electrochemical workstation.

The PVA/KOH gel electrolyte was prepared by dissolving 3 g of PVA in 20 mL of deionized water under magnetic stirring at 90 °C for 2 h until the solution became transparent. Then, a KOH solution (0.3 g/mL) was added dropwise under continuous stirring until a clear, viscous gel was obtained.

The capacitance of each fiber supercapacitor (C_s) was calculated from the galvanostatic charge–discharge (GCD) curves using the following equation:

$$C_s = i/(\mathrm{d}V/\mathrm{d}t), \tag{4}$$

where i, $\mathrm{d}V$, and $\mathrm{d}t$ represent the discharge current, the voltage, and the time, respectively. The specific capacitance corresponding to a single electrode (C_f) was estimated as:

$$C_f = 2C_s \tag{5}$$

The areal (C_f, area) and volumetric (C_f, volume) capacitances of the individual fiber electrodes were obtained by dividing C_f by the electrode's geometric area and volume, respectively. The lateral dimensions of the fibers were determined from SEM analysis for accurate area and volume estimations.

Similarly, the areal ($C_{s,\ area}$) and volumetric ($C_{s,\ volume}$) capacitances of the assembled supercapacitor devices were calculated using:

$$C_{s,\ area} = C_s/Area_s, \tag{6}$$

$$C_{s,\ volume} = C_s/Volume_s, \tag{7}$$

where $Area_s$ and $Volume_s$ denote the total projected area and volume of the supercapacitor device, including the electrolyte and the inter-fiber spacing.

The energy density ($E_{s,\ volume}$) and power density ($P_{s,\ volume}$) of the supercapacitors were calculated using the following relationships:

$$E_{s,\ volume} = C_{s,\ volume}\Delta E^2/(2 \times 3600), \tag{8}$$

$$P_{s,\ volume} = E_{s,\ volume} \times 3600/t_{discharge}, \tag{9}$$

where ΔE is the difference in operating voltage (V) and $t_{discharge}$ is the discharge time.

4.4 Smart Textile Implementation of Core–Shell Nanoyarn Wearable Sensors

The developed Au–TPU core–shell nanoyarns were integrated into a commercial rubber glove to fabricate a wearable capacitive sensor. The sensing unit consisted of two

intersecting nanoyarn electrodes, whose ends were electrically connected to copper wires using silver paste and mechanically fixed to the glove surface with epoxy resin. The TPU shell layer served as a dielectric spacer, and when external pressure was applied, elastic deformation of the TPU shell reduced the gap between the conductive Au cores, resulting in a change in capacitance. Capacitance was measured using an LCR meter (E4980A, Keysight Technologies, USA). Bending motion tests were conducted by controlling finger bending angles at 30°, 60°, and 90°, and the relative capacitance variation was recorded in real time. In touch tests, random forces were applied by finger pressing, and the measured relative capacitance variations were linearly calibrated to the corresponding applied loads. Durability tests were performed under a constant load of 0.3 N for 1000 repetitive loading cycles, during which no significant degradation in signal amplitude was observed.

A 5 × 4 pressure sensor array was implemented based on the mutual capacitance measurement principle using the MSP430FR2633 evaluation board (Texas Instruments, USA). The column yarns were connected to the transmitter electrodes of the integrated circuit (IC), while the row yarns were connected to the receiver electrodes, and each intersection between the two formed an individual sensing element. The yarns and the copper wires were electrically connected using silver paste. The evaluation board was interfaced with an Arduino Uno via Inter-Integrated Circuit (I^2C) communication, which relayed calibration commands and raw count data between the personal computer (PC) and the sensor module. A Python-based graphical user interface (GUI) program on the PC communicated with the Arduino through universal asynchronous receiver–transmitter (UART) connection, transmitting commands and receiving real-time capacitance readings for visualization. Alphabet-shaped stamps ("S," "E," and "N") were fabricated using a fused deposition modeling (FDM) 3D printer (CUBICON Style, Cubicon, Republic of Korea) and resized to 2 cm × 2 cm to apply localized pressure at the target sensing positions. The acquired data were visualized as pressure distributions using a regular-grid interpolation technique, which reconstructs smoothly varying continuous surfaces from evenly spaced datasets, allowing intuitive interpretation of the applied letter-shaped pressure profiles.

Supplementary Information The online version contains supplementary material available at https://doi.org/10.1007/s42765-026-00774-3.

Acknowledgements S.O.K. acknowledges support from the National Research Foundation of Korea (NRF) grant funded by the Ministry of Science and ICT (MSIT) (RS-2025-00521316). S.P.S. acknowledges support from the NRF Creative Challenge Research Grant (RS-2023-00248902). J.S.A. was supported by the Korea Evaluation Institute of Industrial Technology (KEIT) grant funded by the Ministry of Trade, Industry and Energy (MOTIE) (RS-2022-00154781, Development of large-area wafer-level flexible/stretchable hybrid sensor platform technology for form-factor-free highly integrated convergence sensor), the NRF grant funded by the Korean government (MSIT) (RS-2025-00523026), and the IITP (Institute of Information & Communications Technology Planning & Evaluation)-ITRC(Information Technology Research Center) grant funded by the Korea government (Ministry of Science and ICT) (IITP-2026-RS-2023-00258971). J.-H.H. was supported by the Basic Science Research Program through the NRF funded by the Ministry of Education (RS-2025-25414424) and the research fund of Hanbat National University in 2025. I.P. was supported by Alchemist Project grant funded by Korea Evaluation Institute of Industrial Technology (KEIT) & the Korea Government (MOTIE) (Project Number: 1415179744, 20019169) and a National Research Foundation of Korea (NRF) grant funded by the Korean government (MSIT, No. 2021R1A2C3008742).

Author Contributions D.K.: Conceptualization, Methodology, Investigation, Formal analysis, Writing, original draft. S.P.S.: Conceptualization, Methodology, Investigation, Formal analysis, Funding acquisition, Writing, original draft. J.-H.H.: Conceptualization, Methodology, Investigation, Formal analysis, Writing, original draft. O.-S.K.: Investigation, Validation. J.C.: Investigation, Data curation. Y.J.: Methodology, Formal analysis. H.J.: Investigation, Data curation. J.-H.J.: Resources, Validation. Z.-J.Z.: Methodology, Validation. I.P.: Supervision, Project administration, Funding acquisition, Writing, review and editing. S.O.K.: Supervision, Project administration, Funding acquisition, Writing, review and editing. J.A.: Supervision, Project administration, Funding acquisition, Writing, review and editing.

Data Availability The data that support the findings of this study are available from the corresponding author upon reasonable request.

Declarations

Conflict of interest The authors declare that they have no conflict of interest.

References

1. Wang Y, Sun C, Ahmed D. A smart acoustic textile for health monitoring. *Nat Electron*. **2025**;*8*:485.
2. Saifi S, Xiao X, Cheng S, Guo H, Zhang J, Müller-Buschbaum P, Zhou G, Xu X, Cheng HM. An ultraflexible energy harvesting–storage system for wearable electronics and textiles. *Nat Commun*. **2024**;*15*:6546.
3. Kim J, Campbell AS, de Ávila BEF, Wang J. Wearable biosensors for healthcare monitoring. *Nat Biotechnol*. **2019**;*37*:389.
4. Lim H, Choi J, Han C, Kim D, Jin H, Kim M, Kim Y, Yang J, Seo S, Jung J, Ju H, Hong CH, Lee D, Ahn J, Kim HJ. Scalable in-situ fabrication of multimodal electronic skin for intelligent robotics and interactive systems. *npj Flex Electron*. **2026**;*10*:34.
5. Wei R, Li H, Chen Z, Hua Q, Shen G, Jiang K. Revolutionizing wearable technology: advanced fabrication techniques for body-conformable electronics. *npj Flex Electron*. **2024**;*8*:83.
6. Liu K, Ouyang B, Guo X, Guo Y, Liu Y. Advances in flexible organic field-effect transistors and their applications for flexible electronics. *npj Flex Electron*. **2022**;*6*:1.
7. Qian S, Liu M, Dou Y, Fink Y, Yan W. A 'Moore's law' for fibers enables intelligent fabrics. *Natl Sci Rev*. **2023**;*10*:nwac202.
8. Jang H, Ahn J, Jeong Y, Jeon S, Hwang SH, Oh MW, Jeong JH, Park I, Jung YS. Highlighting recent progress in fiber energy harvesters: from working principles to future perspectives. *Adv Sci*. **2026**;*13*: e05784.

9. Aboutalebi SH, Jalili R, Esrafilzadeh D, Salari M, Gholamvand Z, Yamini SA, Konstantinov K, Shepherd RL, Chen J, Moulton SE, Innis PC, Minett AI, Razal JM, Wallace GG. High-performance multifunctional graphene yarns toward wearable all-carbon energy storage textiles. *ACS Nano*. **2014**;*8*:2456.
10. Jin Q, Jiang S, Zhao Y, Wang D, Qiu J, Tang DM, Tan J, Sun DM, Hou PX, Chen XQ, Tai K, Gao N, Liu C, Cheng HM, Jiang X. Flexible layer-structured Bi_2Te_3 thermoelectric on a carbon nanotube scaffold. *Nat Mater*. **2019**;*18*:62.
11. Lan C, Guo M, Li C, Qiu Y, Ma Y, Sun J. Axial alignment of CNTs on fibers enables high-performance conductive fabrics. *ACS Appl Mater Interfaces*. **2020**;*12*:7477.
12. Deforming brittle materials. Nat Mater. **2023**;*22*:1161.
13. Qiu P, Deng T, Chen L, Shi X. Plastic inorganic thermoelectric materials. *Joule*. **2024**;*8*:634.
14. Wang X, Zhang Y, Zhao Y, Li G, Yan J, Yu J, Ding B. A general strategy to fabricate flexible oxide ceramic films. *Adv Funct Mater*. **2021**;*31*:2103989.
15. Jang KI, Li K, Chung HU, Xu S, Jung HN, Yang Y, Kwak JW, Jung HH, Song J, Yang C, Wang A, Liu Z, Lee JY, Kim BH, Kim JH, Lee J, Yu Y, Kim BJ, Jang H, Yu KJ, Kim J, Lee JW, Jeong JW, Song YM, Huang Y, Zhang Y, Rogers JA. Self-assembled three-dimensional network designs for soft electronics. *Nat Commun*. **2017**;*8*:15894.
16. Wu J, Liu ZJ, Song J, Huang Y, Hwang KC, Zhang YW, Rogers JA. Stretchability of encapsulated electronics. *Appl Phys Lett*. **2011**;*99*:061911.
17. Chen Y, Zhang Y, Liang Z, Cao Y, Han Z, Feng X. Flexible inorganic bioelectronics. *npj Flex Electron*. **2020**;*4*:2.
18. Peng J, Snyder GJ. A figure of merit for flexibility. *Science*. **2021**;*373*:1017.
19. Liu S, He J, Rao Y, Dai Z, Ye H, Tanir JC, Li Y, Lu N. Conformability of flexible sheets on spherical surfaces. *Sci Adv*. **2023**;*9*:eadf2709.
20. Jang H, Ahn J, Jeong Y, Ha JH, Jeong JH, Oh MW, Park I, Jung YS. Flexible all-inorganic thermoelectric yarns. *Adv Mater*. **2024**;*36*:2408320.
21. Ahn J, Jeong Y, Kang M, Ahn J, Sasikala SP, Yang I, Ha JH, Hwang SH, Jeon S, Gu J, Choi J, Kang BH, Kim SO, Kim S, Choi J, Jeong JH, Park I. Nanoribbon yarn with versatile inorganic materials. *Small*. **2024**;*20*:2311736.
22. Ha JH, Yang J, Kim D, Lee W, Yun C, Hwang SH, Jeon S, Choi J, Lim H, Kim M, Kim D, Park SA, Choi J, Song JW, So S, Ahn J, Jeong JH. SERS sensor integrated in stretchable and antimicrobial wrapper for food quality monitoring and preservation. *Small*. **2025**;*21*:2501808.
23. Ahn J, Gu J, Jeong Y, Ha JH, Ko J, Kang B, Hwang SH, Park J, Jeon S, Kim H, Jeong JH, Park I. Nanotransfer-on-things: from rigid to stretchable nanophotonic devices. *ACS Nano*. **2023**;*17*:5935.
24. Kang BH, Ha JH, Kwon Y, Jeon S, Lee D, Kang B, Hwang SH, Ahn J, Jeong JH, Park I. Versatile water-floated nanostructures for three-dimensional nanotransfer printing. *Nat Commun*. **2026**;*17*:4588.
25. Ahn J, Sasikala SP, Jeong Y, Kim JG, Ha JH, Hwang SH, Jeon S, Choi J, Kang BH, Ahn J, Jeong JH, Kim SO, Park I. High-energy-density fiber supercapacitors based on transition metal oxide nanoribbon yarns for comprehensive wearable electronics. *Adv Fiber Mater*. **2024**;*6*:1927.
26. Zhou X, Fang S, Leng X, Liu Z, Baughman RH. The power of fiber twist. *Acc Chem Res*. **2021**;*54*:2624.
27. Li Y, Guo F, Hao Y, Gupta SK, Hu J, Wang Y, Wang N, Zhao Y, Guo M. Helical nanofiber yarn enabling highly stretchable engineered microtissue. *Proc Natl Acad Sci USA*. **2019**;*116*:9245.
28. Ha JH, Kim JY, Kim D, Ahn J, Jeong Y, Ko J, Hwang S, Jeon S, Jung Y, Gu J, Han H, Choi J, Lee G, Bok M, Park SA, Cho YS, Jeong JH, Park I. Multifunctional micro/nanofiber-based dressing patch with healing, protection, and monitoring capabilities for advanced wound care. *Adv Mater Technol*. **2023**;*8*:2201765.
29. Shaker A, Khedewy AT, Hassan MA, Abd El-Baky MA. Thermo-mechanical characterization of electrospun polyurethane/carbon-nanotubes nanofibers: a comparative study. *Sci Rep*. **2023**;*13*:17368.
30. Galuppi L, Pasquali M, Royer-Carfagni G. The effective tensile and bending stiffness of nanotube fibers. *Int J Mech Sci*. **2019**;*163*:105089.
31. Raischel F, Kun F, Herrmann HJ. Fiber bundle models for composite materials. In: Proceedings of the conference on damage in composite materials: simulation and non-destructive testing, 18–19 Sep 2006. Stuttgart, Germany. **2006**.
32. Gul O, Ahn J, Kim HJ, Yu X, Park I. Mechanochemically activatable liquid metal powders for sustainable, reconfigurable, and versatile electronics. *Adv Funct Mater*. **2026**;*36*:e27396.
33. Sambles JR, Elsom KC, Jarvis DJ. The electrical resistivity of gold films. *Philos Trans R Soc Lond A Math Phys Sci*. **1982**;*304*:365.
34. Lee SE, Moon KS, Sohn Y. Temperature dependence of contact resistance at metal/MWNT interface. *Appl Phys Lett*. **2016**;*109*:021605.
35. Tang Z, Jia S, Wang F, Bian C, Chen Y, Wang Y, Li B. Highly stretchable core–sheath fibers via wet-spinning for wearable strain sensors. *ACS Appl Mater Interfaces*. **2018**;*10*:6624.
36. Abdel Haleem A, Enjoji H, Gu K, Miwa T, Kuroda Y, Orikasa Y, Uchiyama T, Uchimoto Y, Mitsushima S. Accelerated durability assessment and a proposed degradation mechanism of NiCoOx OER catalysts under simulated intermittent renewable power: insights from XAS. *ACS Appl Mater Interfaces*. **2025**;*17*:61929.
37. Yuan S, Xia M, Liu Z, Wang K, Xiang L, Huang G, Zhang J, Li N. Dual synergistic effects between Co and Mo_2C in Co/Mo_2C heterostructure for electrocatalytic overall water splitting. *Chem Eng J*. **2022**;*430*:132697.
38. Zhang SL, Guan BY, Lu XF, Xi S, Du Y, Lou XW. Metal atom-doped Co3O4 hierarchical nanoplates for electrocatalytic oxygen evolution. *Adv Mater*. **2020**;*32*:2002235.
39. Jiang H, He Q, Li X, Su X, Zhang Y, Chen S, Zhang S, Zhang G, Jiang J, Luo Y, Ajayan PM, Song L. Tracking structural self-reconstruction and identifying true active sites toward cobalt oxychloride precatalyst of oxygen evolution reaction. *Adv Mater*. **2019**;*31*:1805127.
40. Huang J, Sun Y, Du X, Zhang Y, Wu C, Yan C, Yan Y, Zou G, Wu W, Lu R, Li Y, Xiong J. Cytomembrane-structure-inspired active Ni–N–O interface for enhanced oxygen evolution reaction. *Adv Mater*. **2018**;*30*:1803367.
41. Qin K, Wang L, Wen S, Diao L, Liu P, Li J, Ma L, Shi C, Zhong C, Hu W, Liu E, Zhao N. Designed synthesis of NiCo-LDH and derived sulfide on heteroatom-doped edge-enriched 3D rivet graphene films for high-performance asymmetric supercapacitor and efficient OER. *J Mater Chem A*. **2018**;*6*:8109.
42. Yu D, Goh K, Wang H, Wei L, Jiang W, Zhang Q, Dai L, Chen Y. Scalable synthesis of hierarchically structured carbon nanotube-graphene fibres for capacitive energy storage. *Nat Nanotechnol*. **2014**;*9*:555.
43. Yu Z, Moore J, Calderon J, Zhai L, Thomas J. Coil-type asymmetric supercapacitor electrical cables. *Small*. **2015**;*11*:5289.
44. Ren J, Li L, Chen C, Chen X, Cai Z, Qiu L, Wang Y, Zhu X, Peng H. Twisting carbon nanotube fibers for both wire-shaped micro-supercapacitor and micro-battery. *Adv Mater*. **2013**;*25*:1155.

45. Sasikala SP, Lee KE, Lim J, Lee HJ, Koo SH, Kim IH, Jung HJ, Kim SO. Interface-confined high crystalline growth of semiconducting polymers at graphene fibers for high-performance wearable supercapacitors. *ACS Nano*. **2017**;*11*:9424.
46. Cho S, Ha JH, Moon J, Ahn J, Kim G, Ma X, Fan K, Song R, Lee D, Han H, Ahn J, Oh Y, Choi W, Oh YS, Hwang S, Jeon S, Jeong Y, Kim D, Park SA, Jeong JH, Gao W, Park I. Wireless, battery-free, optoelectronic, multi-modal sensor integrated with colorimetric dressing for diabetic ulcer management. *Adv Funct Mater*. **2026**;*36*:e32167.
47. Lee K, Gul O, Kwon Y, Jeong J, Cho S, Ahn J, Yu J, Kim C, Lee D, Han H, Lee B, Choi J, Ha JH, Jeong Y, Kang K, Javey A, Ahn J, Park I. Smarter sensors through machine learning: historical insights and emerging trends across sensor technologies. *Adv Funct Mater*. **2026**;*36*:e19859.
48. Kim H, Cho S, Han C, Ahn J, Lee D, Jang S, Lee G, Lee K, Han H, Ha JH, Ahn J, Jeong Y, Choi J, Park I. Modular tactile sensing platform with sequential optical sampling for human-robot interfaces. *Device*. **2026**;*4*:101081.

Publisher's Note Springer Nature remains neutral with regard to jurisdictional claims in published maps and institutional affiliations.

Springer Nature or its licensor (e.g. a society or other partner) holds exclusive rights to this article under a publishing agreement with the author(s) or other rightsholder(s); author self-archiving of the accepted manuscript version of this article is solely governed by the terms of such publishing agreement and applicable law.